Experimental and numerical investigation of the influence of roller bending in rectangular hollow section steel arches

Ilias D. Thanasoulas, Cyril Douthe, Charis J Gantes, Xenofon A. Lignos

Experimental and numerical investigation of the influence of roller bending in rectangular hollow section steel arches

Ilias D. Thanasoulas[1], Cyril E. Douthe[2], Charis J. Gantes[1], Xenofon A. Lignos[1]

[1] Institute of Steel Structures, School of Civil Engineering, National Technical University of Athens, Greece

[2] Laboratoire Navier, Ecole des Ponts ParisTech, IFSTTAR, CNRS, France

Abstract

An experimental and numerical investigation of the influence of residual stresses due to curving in rectangular hollow section steel arches on the overall structural behaviour is presented. Twelve circular arch specimens, grouped in two sets of curvatures, are tested under tension and compression loading. Detailed finite element models are used to simulate in detail the curving procedure as well as the experimental tests and implicit static analyses accounting for geometric and material nonlinearities are carried out. Experimental and numerical results are compared in terms of load-displacement equilibrium paths, strain-gauge measurements and deformed shapes. Overall, a quite good quantitative and qualitative agreement is achieved between FEA and experimental results, demonstrating the capability of the developed finite element models to reliably estimate the residual stress distribution caused by the forming process. The numerically estimated residual stresses are presented for the two sets of specimens, providing good agreement with the models proposed in the literature. Extended plastification at the bottom flange edges of the arches is observed, reducing significantly the member's remaining ductility; the developed accumulated plastic strains are found to be remarkably larger than the longitudinal strains that are expected according to the classic beam theory. Maximum discrepancies of approximately 10% are reported in the structural response of the arches depending on whether the estimated locked-in stress distributions are taken into account or not.

Keywords: Steel arches; Residual stresses, Roller bending; Cold-forming; Curving process

1. Introduction

The technological progress of the last few decades regarding steelmaking and forming techniques, as well as the advances in computational tools employed in engineering analysis, have influenced the design and construction of steel structures. Curved structural steel members are used more and more in modern construction, mainly due to their improved aesthetics compared to conventional geometries. The circular arch comprises the simplest curved geometry, which is customarily used to cover large spans due to its ability to carry loads largely in compression rather than bending. Typical applications of arch elements can be seen in large span roofs, bridges, stadiums, atriums etc.

Curved constructional steels are manufactured from initially straight members which are subjected to bending in order to meet the desired curvature [1-3]. Five curving methods are typically employed in the steel industry, namely: (i) “Roller bending”, (ii) “Incremental bending”, (iii) “Hot bending”, (iv) “Rotary-draw bending” and (v) “Induction bending”. The “Roller bending” or “Pyramid rolling” method as it is also called because of the bending machine’s pyramid arrangement (Fig. 1), is the most common method of curving constructional steels since it is usually less costly than the others [4]. It is a cold-forming process where a steel member passes iteratively through three rollers, causing plastic deformations along its entire length. In each subsequent iteration, the roller in the middle moves towards the other two, in order to adjust the applied curvature. Curved elements with noncircular geometries can also be manufactured with this process, such as elliptical forms, combinations of circular and elliptical shapes or S-type curves.

Figure 1: Roller bending machine for constructional steel.

Generally, the minimum achieved radius of curvature is limited by the maximum magnitude of cross-sectional distortion which is allowed to take place during the bending process. Special techniques are used in order to minimize this phenomenon, such as filling the hollow sections with mandrels, or utilizing auxiliary rolls on the tension flanges of open cross-sections in order to provide additional restraint against local flange bending and web buckling. The minimum bending radius for cold bending of hollow steel sections has

been assessed in some early studies [5-7], based on a series of experiments and using limits of 1% or 2% concerning the permitted wall deformations. Additionally, limits regarding the minimum radius of curvature for steel members have been proposed in [8]; the minimum radius is proposed to be between 10 and 14 times the depth of the member for cross-sections up to a nominal depth of 750 mm (30 in.), while deeper members may require a larger minimum radius. However, the aforementioned considerations may not be strictly employed since distortional effects continue to be reduced with advances in bending equipment and techniques.

Locked-in stresses affect the overall behavior of every structural element, having considerable effect on the brittle fracture, fatigue, buckling strength and inducing premature yielding of the cross-section [9]. Residual stresses of hot-rolled and cold-formed cross-sections, which are caused by uneven cooling and differential plastic deformations respectively, have been investigated in numerous experimental studies [10-16]. The available analytical expressions used to estimate the locked-in stress distributions for several types of cross-sections have been summarized in a recent review article [17]. However, when an initially straight member made of a hot-rolled or cold-formed profile is curved into the desired shape, most of the section exhibits yielding. Thus, the existing residual stress pattern due to the cross-section forming is replaced by a new residual stress pattern due to curving, which is considered independent of the initial one.

A theoretical model for predicting the residual stress distribution caused by cold-bending has been proposed by Timoshenko [18], as a function of the steel's yield stress fy and the ratio α between the plastic and elastic section modulus; the predicted stress distribution is depicted for a typical I and a Rectangular Hollow (RH) section in Fig. 2. This model is based on the Euler-Bernoulli beam theory by aggregating uniaxial stresses from inelastic bending and elastic spring-back and thus, 3-dimensional effects emanating from the theory of plates are neglected. Residual stress measurements have been carried out by Spoorenberg et al. [19] on roller bent wide flange sections using the sectioning method; specimens of different dimensions, steel grades, and bending curvatures were examined. The obtained residual stress distribution differed significantly from Timoshenko's distribution, exhibiting stress concentration at the web-to-flange junctions. Detailed finite element simulations of the curving process followed next [20] in order to validate the developed numerical models with experimental results; an analytical model predicting the residual stress of wide flange sections subjected to bending was proposed in [21]. Another computational study concerning roller bent rectangular hollow sections has been performed in [22], where the full interaction between the bending machine and the work pieces was modeled and a numerical parametric study was carried out; an analytical model for predicting the locked-in stresses of rectangular hollow sections subjected to bending has been proposed as well.

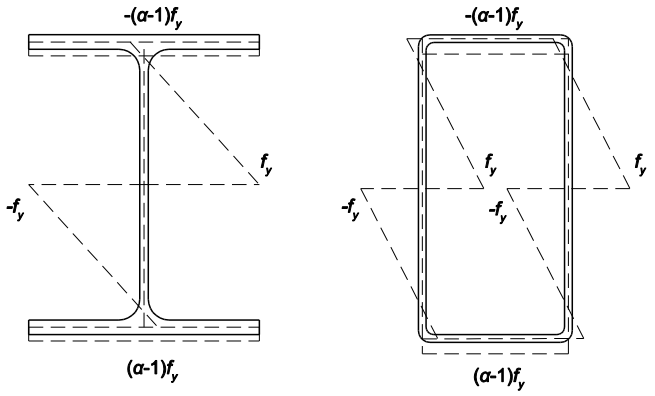

Figure 2: Theoretical residual stress distribution for roller bent I (left) and RH (right) sections, proposed by Timoshenko.

The influence of residual stresses on the structural response of steel arches has been assessed until now in several studies [23-25], by employing patterns concerning straight members. However, the way in which residual stresses influence the behaviour depends on their distribution over the cross-section, which is considerably different in the case of curved members than in straight members [26]. An experimental and numerical investigation of the encountered residual stresses in rectangular hollow section steel arches along with their influence on the overall structural behaviour is performed in the present study. Twelve circular arch specimens, grouped in two sets of curvatures, are tested under tension and compression loading. Finite element models are used to simulate the preceded curving procedure as well as the experimental tests and implicit static analyses accounting for geometric and material nonlinearities are carried out in the general purpose finite element software ADINA [27]. Experimental and numerical results are compared in terms of load-displacement equilibrium paths, strain-gauge measurements and deformed shapes. The numerically estimated residual stresses are compared with the models proposed in the literature and finally, the effect of residual stresses on the overall structural behaviour is assessed through the comparison of numerical models in which the estimated locked-in stress distributions are either included or omitted.

2. Test specimens and experimental set-up

2.1 Geometric characteristics of specimens

A total number of twelve circular steel arches were tested at the Institute of Steel Structures in the School of Civil Engineering of the National Technical University of Athens (Fig. 3); the forming process was carried out at EMEK SA facilities. A Rectangular Hollow Section (RHS) 100 x 50 x 5 mm of S355 steel quality was chosen for all specimens, which were curved along their weak axis in order to exhibit higher out-of-plane stiffness. The first set of six arches were designed with radii of curvature equal to 3.71 m (referred

thereinafter as high arches), while the second set of six arches were designed with radii of curvature equal to 4.10 m (referred thereinafter as low arches). Both high and low arches were designed to cover the same horizontal span of 4725 mm. Three compression and three tension tests were performed for each set, inducing opening and closing bending moments at crown respectively; the different test configurations for all arches are summarized in Table 1.

Figure 3: Twelve circular steel arches received for testing at the Institute of Steel Structures of NTUA.

Table 1. Test configurations.

Curvature	Tension tests	Compression tests
High arch (R = 3.71 m)	3	3
Low arch (R = 4.10 m)	3	3

Steel arches manufactured by the roller bending method usually exhibit a large amount of geometric imperfections and the achieved in-plane curvature is not ideally uniform. Six measurements were undertaken in each arch in order to evaluate the exact dimensions of the specimens, including the length of the horizontal span (L), as well as the height at five locations along the member ($h1$-$h5$), shown in Fig. 4; the measured dimensions of the high and low arches and the corresponding theoretical values are summarized in tables A1 and A2 of Appendix A. The mean horizontal span was measured to be approximately 7 mm longer for the high arches and 13 mm shorter

for the low arches, relatively to the theoretical ones, while the mean middle height was found 3mm larger and 13 mm shorter for the high and low arches respectively. A maximum difference of approximately 9 mm between the heights of the first and second half of the arches was measured, inducing loss of symmetry. The best fitting radius and the deriving deviations of each specimen's curvature were calculated by employing the least square method and results are presented in tables A3 and A4 of Appendix A; the average fitting radii of the high and low arches were estimated equal to 3.73 m and 4.03 m respectively.

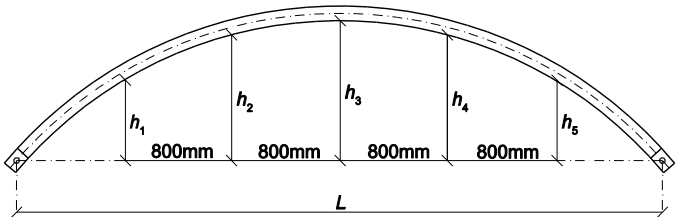

Figure 4: Dimension measurements of arch specimens.

2.2 Material characteristics of specimens

The mechanical properties of steel have been extracted through tensile coupon tests of three indicative specimens (Specimens 2, 4 and 10). Coupons were formed from the initially straight elements prior to the curving process, in order to avoid locked-in stresses caused by roller bending. The coupon geometry and testing procedure were according to EN ISO 6892-1:2009 [28]. A view of a typical coupon during the test is illustrated in Fig. 5

Figure 5: Tensile coupon test.

Typical tension tests provide forces and displacements which are used to compute engineering stresses (σ_e) and engineering strains (ε_e). Therefore, it is necessary to convert engineering stress-strain data to true stress-strain data. The corresponding true stress (σ_t) and true strain (ε_t) can be calculated according to Eq. (1) and (2):

$$\sigma_t = \sigma_e(1 + \varepsilon_e) \quad (1)$$

$$\varepsilon_t = \ln(1 + \varepsilon_e) \quad (2)$$

The modulus of elasticity obtained from the coupon tests was found to be equal to 205 GPa, as expected for constructional steel. The proportional limit was equal to 270 MPa and the yield stress equal to 470MPa, corresponding to a strain of 0.01 % and 0.2 %, respectively. The ultimate tensile stress occurred 550 MPa at a maximum strain of 10.1 %. The complete stress -strain curves obtained from the three tensile coupon tests are given in Fig 6; very good agreement is reported between them, confirming that the quality of steel specimens is S355. However, it is remarkable that the transition between the elastic and the plastic domains is very smooth, on the contrary to what is generally assumed. It is also noteworthy that the material exhibits premature yielding; the proportional limit is approximately 25 % lower than the expected yield stress (355 MPa). This behaviour along with the limited ductility which is observed are considered to be consequence of the forming process of the rectangular hollow section, which caused significant hardening to the material and high residual stresses, both longitudinally and transversally [29].

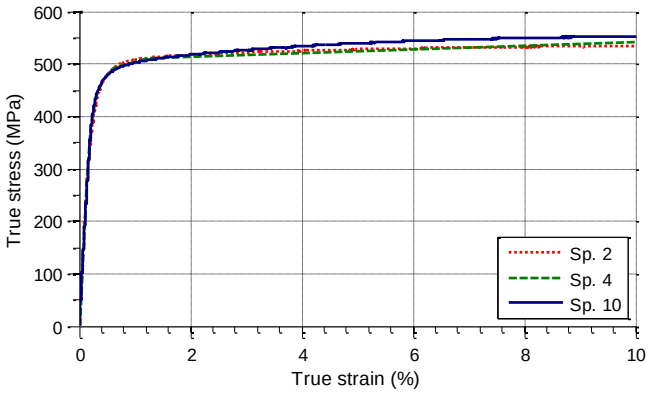

Figure 6: True stress-strain curves of steel material.

2.3 *Experimental set-up*

An appropriate test layout was designed for the execution of the experimental tests, including configurations for the supports and load application of the arch specimens. The specimens were placed to the laboratory testing frame and hinged using pins in both ends.

All arches were reinforced locally at their ends, by welding 10 mm thick plates at the webs of the RHS section, in order to avoid local yielding in the vicinity of the pivot axes. The distance between the hinges was designed to be 4725 mm in all tests. Since the initial arches' span was not the same for all specimens and they did not fit exactly within the position of the hinges (high arches were in general 7 mm longer while low arches were 13 mm shorter), a proper displacement was imposed at the one arch's end, through a temporary sliding system, in order to open or close the arch and bring the hinge to the right position before placement of the pin. Lateral supports were added at the thirds of the span, providing additional out-of-plane protection, since numerical simulations demonstrated that the first out-of-plane buckling load was relatively close to the ultimate bearing capacity of the arches. The inner face of these supports was covered by Teflon™ foils in order to reduce friction between the arch and the support. The laboratory testing frame along with the employed configurations are illustrated in Fig. 7; the hinged supports at the arches' ends are shown in Fig. 8

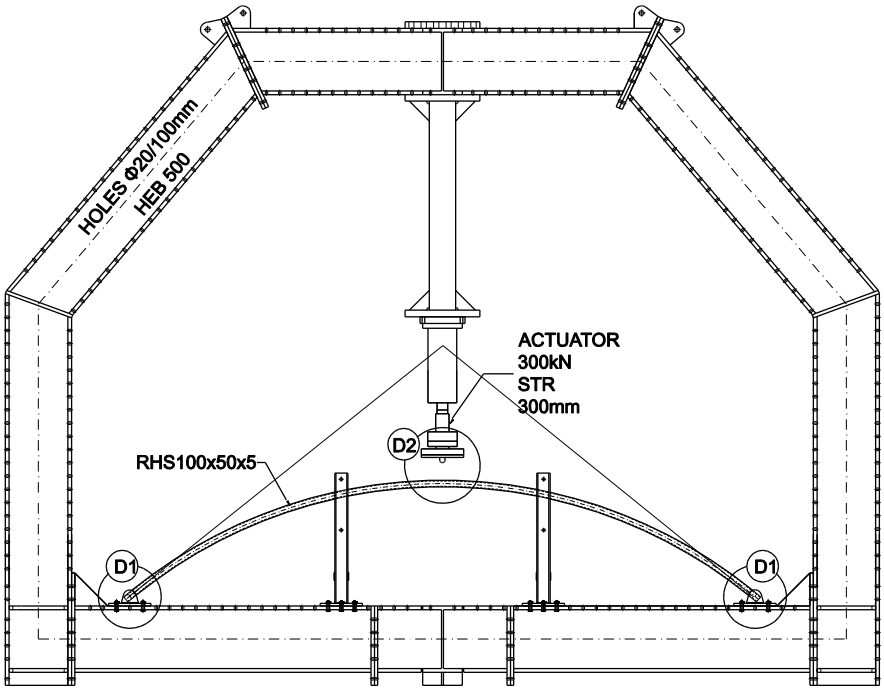

Figure 7: Laboratory testing frame and test configuration.

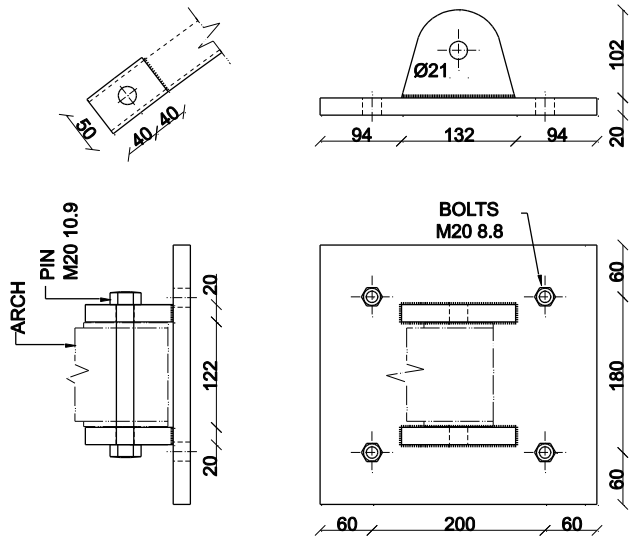

Figure 8: Plan view and lateral views of the main support (D1).

158

159 Compression and tension tests were performed using a 300 kN hydraulic actuator. The load was imposed to the arch crown through
160 a 30 mm thick loading plate, on which half of a cylinder with diameter 48mm was welded (referred thereinafter as loading cylinder). In
161 the compression test configuration, the loading plate was fixed directly to the actuator by bolts, whereas in the tension test configuration,
162 it was inverted and attached to the actuator through four rods. All auxiliary elements were designed to have sufficient overstrength and
163 stiffness, in order to ensure uniform load application on the specimen and consequently avoid any undesirable local failure of the tube.
164 Views of the loading plates used for the tension and compression tests are illustrated in Fig 9.

165

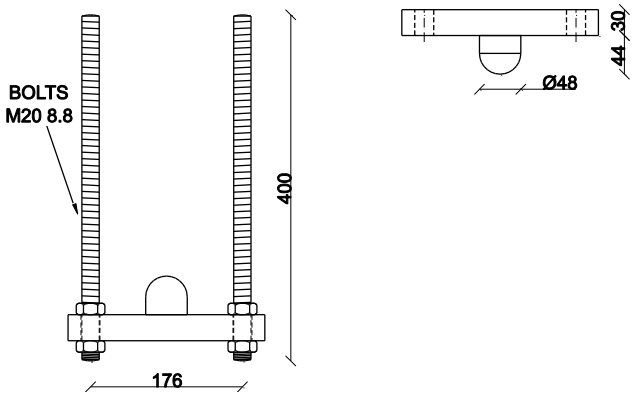

Figure 9: View of the loading plates (D2) for the tension (left) and compression

(right) tests.

166

167 The performed tests were displacement controlled and followed the same protocol; a first loading step up to 20 mm was executed,
168 followed by an unloading step back to 10 mm, before the final loading up to 80 mm and 95 mm for the tension and the compression

tests, respectively. The magnitude of the maximum displacement was sufficient for reaching the ultimate bearing capacity of the arches, while the small cycle between 10 mm and 20 mm (within the elastic range) was aimed at investigating the elastic properties of the specimens, while remaining in the domain where the clearances did not influence the tests. The imposed displacement along with the reaction force were measured by a displacement-cell and a load-cell respectively, mounted on the actuator's head.

Three Individual Linear Variable Differential Transformers (LVDTs) were installed to measure the specimen's vertical displacement at a distance of 150 mm left of the crown and assess the deflection and torsional rotation near the top. The deflected shape was also captured by an inclined LVDT on each side, placed perpendicularly to the arch cross-section at a horizontal distance of 700 mm from the arches' ends (their position was selected on the basis of linear static analyses and corresponds approximately to the point of maximal deflection in the opposite direction of that at crown). Four Strain Gauges (SGs) consisting of two 90° tee rosettes and two linear gauges, were set on each specimen in order to measure the developed longitudinal and transverse strains at a cross-section located 150 mm on the right of the crown. The two rosettes were placed in the middle of the top and bottom flanges, while the two linear gauges were placed on the top flange edges, in order to assess the uniformity of the stress distribution. The experimental set-up along with the employed measuring devices are depicted in Fig. 10.

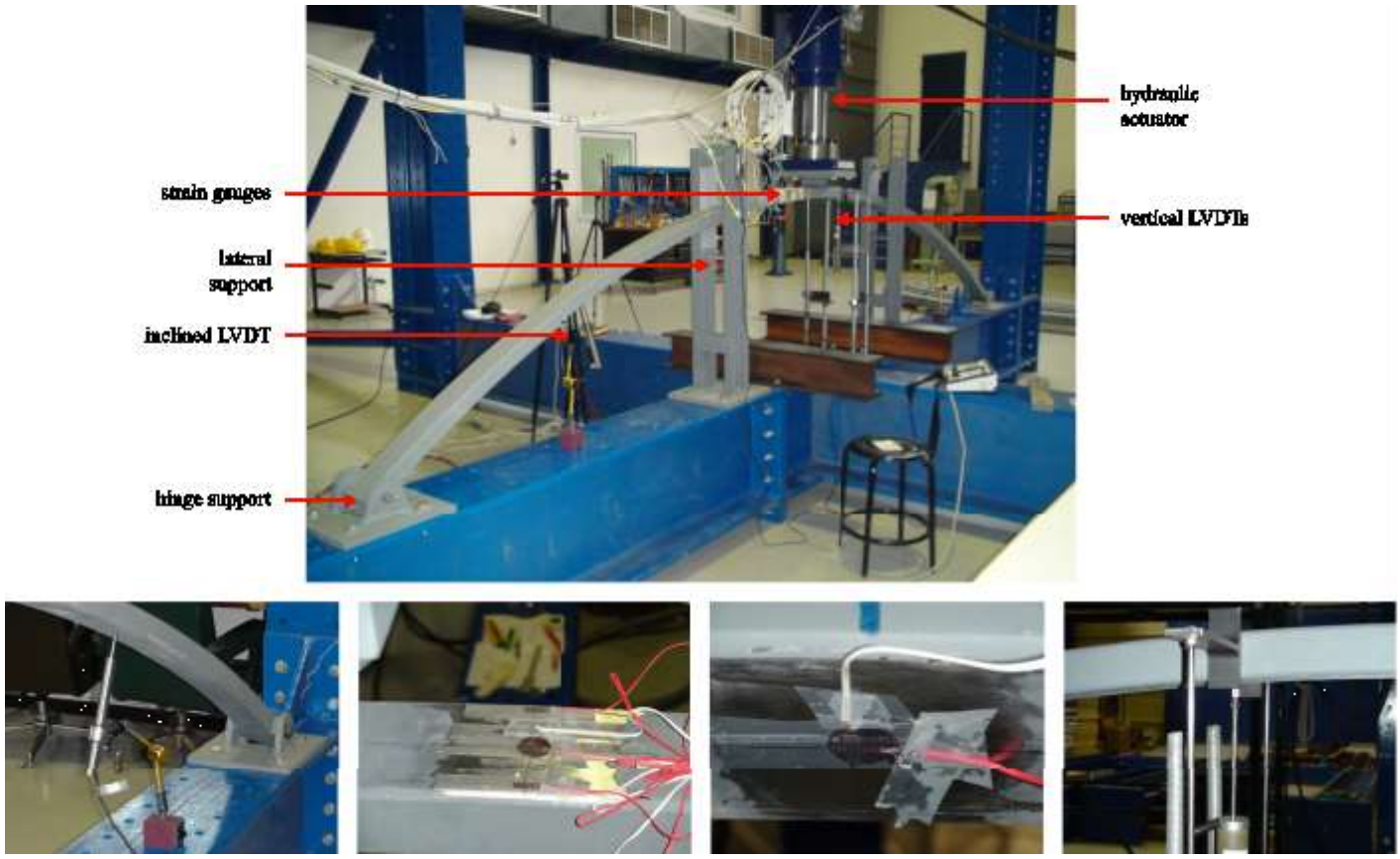

Figure 10: View of the experimental set-up (top) and the measuring devices (bottom) in the following order:

inclined LVDT, top flange SG, bottom flange SG, vertical LVDTs.

3. Numerical modelling of the experiments

The general purpose finite element software ADINA was employed for the numerical simulation of the experiments. Implicit static analyses accounting for geometric and material nonlinearities were carried out using the Newton – Raphson solution algorithm. The implementation of Geometry and Material Nonlinear Analyses (GMNA) considered the practical aspects of Finite Element Method (FEM) presented in [30]. Large displacement and large strain formulations were employed since local or global buckling of the specimens were found critical during the tests and the developed plastic strains due to the curving process were significant. Locked-in stresses emanating from the forming process of the rectangular hollow section were not considered in the analyses since it is generally assumed that these residual stresses are removed and replaced by new during the curving process.

In order to maintain an acceptable level of accuracy and at the same time reduce the computational effort, numerical modeling was performed in three steps: (i) the hinge support was modeled first, in order to estimate the stiffness provided to the arch specimens, (ii) detailed simulation of the curving process was performed then, in order to obtain a reliable residual stress pattern and finally, (iii) the compression and tension tests of the arches were simulated, considering the computed residual stress distribution and stiffness of the supports.

3.1 Simulation of the support assembly

In order to estimate the stiffness provided by the hinged support to the arch specimens, a detailed numerical model of the actual support configuration was developed. The numerical model, consisting of (i) a M20 10.9 pin, (ii) two vertical plates of steel S355 and (iii) a part of the RHS 100 x 50 x 5 mm, was built using 8-node brick 3d-solid finite elements, as shown in Fig. 11. Bilinear elastic-plastic material models were used for the simulation of all parts composing the assembly; the mechanical properties obtained from the tensile coupon tests (Section 2.2) were used for the RHS segment while the characteristic values of the mechanical properties were used for the pin and the plates, in absence of more accurate experimental data. Appropriate contact elements were introduced at the interfaces between adjacent parts, taking into account the design geometric tolerances inside the assembly; the Coulomb friction coefficient of the contacting surfaces was taken equal to 0.3.

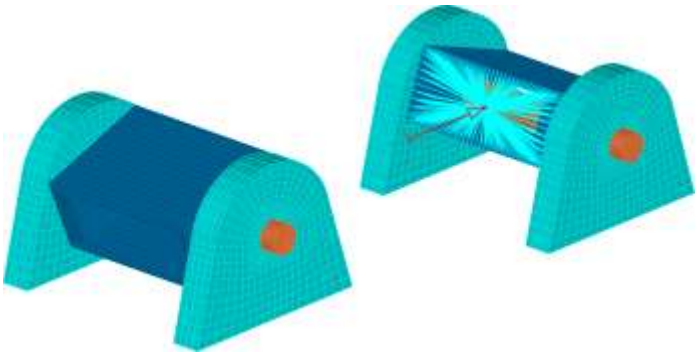

Figure 11: Simulation of the arch's hinged support with 3d finite elements.

The vertical steel plates were fixed at the base and a horizontal force, causing either compression (negative) or tension (positive) for the arch, was applied on the cross-sectional centroid with the use of rigid links; the other degrees of freedom of the cross-sectional centroid were restrained. The estimated horizontal stiffness for the low and high arches, obtained from GMN analyses, is presented in Fig. 12; the difference in the response between the two cases is caused by the consideration of different initial tolerances, since high arches were compressed while low arches were tensioned in order to fit the span of the experimental setup. Tolerances in the vertical direction were found to have negligible effect on the overall behaviour of arches, and thus the vertical support stiffness was assumed as rigid.

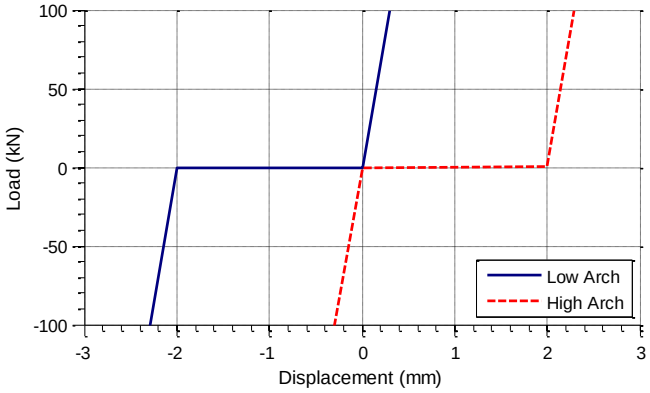

Figure 12: Support's stiffness at the horizontal direction.

3.2 Simulation of the curving process

Subsequently, aiming at obtaining a realistic distribution of the encountered residual stresses in the arch specimens, the curving process of initially straight segments was numerically simulated. Two different numerical models were developed in order to simulate

the curving procedure of the low and high arches consisting of rectangular hollow sections. The straight length of the beams was assumed to be equal to the corresponding curved length after the bending process and based on the average measured dimensions for each set of specimens. A uniform and sufficiently dense mesh with 4-node shell elements and five integration points at the element thickness direction was employed in order to model reliably the elastoplastic behavior of the RHS thin-walled plates; a bilinear material model based on the mechanical properties obtained from the tensile coupon tests (Section 2.2) was used.

The curving process of an initially straight beam can be simulated numerically either by applying opposite prescribed rotations at the beam's ends or by modelling the full interaction with the bending rolls. Less computational effort is required in the first case, where the obtained locked-in stresses are found to be more consistent with the Timoshenko stress distribution of Fig. 1. The numerical simulation in the second case is much more sophisticated and computationally demanding but literature findings [20, 22] agree well that a different and more reliable locked-in stress distribution is provided. Both methods were employed in order to perform some preliminary analyses and to evaluate the results. It was confirmed that the residual stress patterns of a rectangular hollow section steel arch differed significantly; a comparison of the locked-in stress distributions provided in both cases is depicted in Fig. 13.

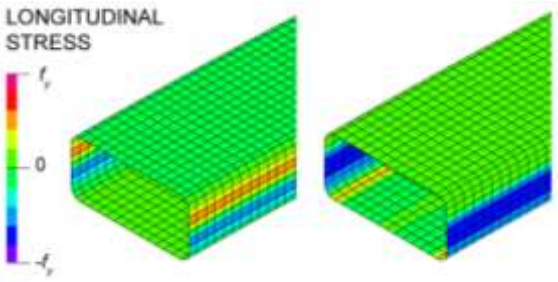

Figure 13: Comparison of the longitudinal locked-in stresses provided by applying prescribed rotations (left) and by modelling the full interraction (right).

To that and, the second approach was eventually adopted in the present study and the full interaction between the rolls and the work piece was simulated. Three cylindrical rolls of 300 mm diameter and pyramid arrangement were modelled with shell elements. The distance between the centres of the outer rolls was taken equal to 900 mm. Rigid elements were used to connect the nodes of each cylinder to its centre, in order to apply the prescribed rotations and displacements. Appropriate contact elements were introduced between the contacting interfaces of the rolls and the beam and the Coulomb friction coefficient of the contacting surfaces was taken equal to 0.3; the rigid target algorithm was employed for the solution of the contact-element equations. Large strain and displacement formulations were employed for the GMNA. The load step required in order to achieve uniform curvature along the segment, mainly depends on the number of elements at the longitudinal beam direction; in the present study a sensitivity analysis was performed in order to select the appropriate load step magnitude.

Numerical simulation of the curving procedure is performed in three stages, which are illustrated schematically in Fig. 14. Firstly, (i) a prescribed displacement at the middle roller is applied towards the beam, causing plastic deformations at this point. Subsequently, (ii) a prescribed rotation is applied at the centre of one roller (i.e the middle one) and, through contact traction, the beam is feeded inside the bending machine causing uniform plastification over its entire length. The angular speed has to be controlled by a single roller, since it is different between the three rollers; thus rotating of the other rollers is left unrestrained. Finally, (iii) when the entire work piece has been feeded inside the bending machine, the middle roller is moved downwards, releasing the beam. At the end of this procedure, the beam's edges will not have been bent to the desired curvature since they have not passed entirely through the machine; these regions with length equal to the distance between the centres of the outer rollers, comprise waste material and are cut-off. To that end, the initial straight length of the beam is modelled to be larger by twice the length of the bending machine.

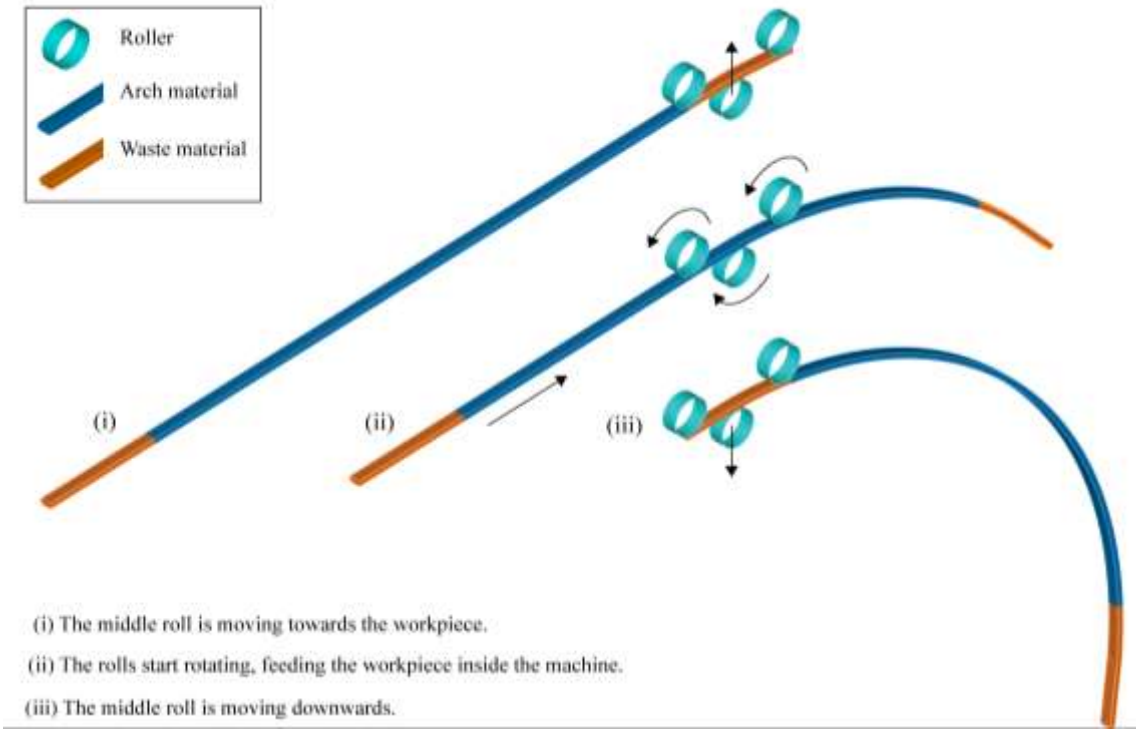

Figure 14: Numerical simulation of roller bending process.

Due to the highly non-linear character of the roller bending process it is hard to accurately predict in advance the required displacement of the middle roller in order to arrive at the exact specified radius of curvature. Thus, in practice multiple passes through the rolls are needed to successfully bend a beam. In the numerical simulations, only a single forming pass was analyzed, assuming that the residual stresses are identical for single- and multiple pass bending. An analytical formula for estimating the required displacement is proposed in the current study, based on the principle of virtual work and assuming triangular moment distribution of the beam segment

between the rollers. For the straight beam subjected to three point bending, shown in Fig. 15, the principle of virtual work is expressed by Eq. 3.

$$M_{pl} \cdot \varphi = F \cdot d \quad (3)$$

where:

M_{pl} = section's plastic moment capacity

φ = plastic angle of rotation

F= acting force at the middle cross-section

d= residual deflection at the middle cross-section

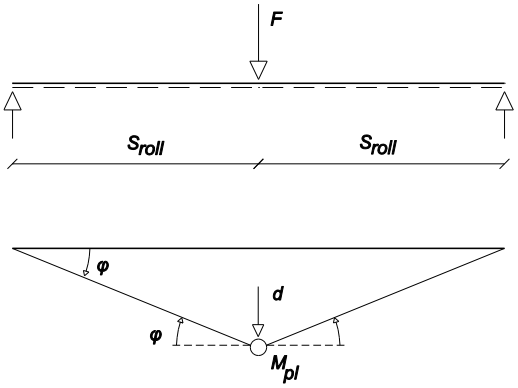

Figure 15: Method of virtual work for a beam subjected to three point bending

After the development of a plastic hinge at the middle of the simply-supported beam, the acting force F can be calculated by Eq. 4.

$$F = \frac{2M_{pl}}{S_{roll}} \quad (4)$$

where S_{roll} is the horizontal distance between the rollers.

The plastic angle of rotation is determined by the integration of the plastic curvature *(k)* along the plastic hinge length (L_{pl}), according to Eq. 5.

$$\varphi = k \cdot L_{pl} \quad (5)$$

The plastic hinge length (L_{pl}) of the beam segment shown in Fig. 16, can be calculated as a function of the horizontal distance between the rollers and the cross-sectional elastic (W_{el}) and plastic (W_{pl}) moment resistances, according to Eq. 6.

$$L_{pl} = 2S_{roll}\frac{(W_{pl} - W_{el})}{W_{pl}} \quad (6)$$

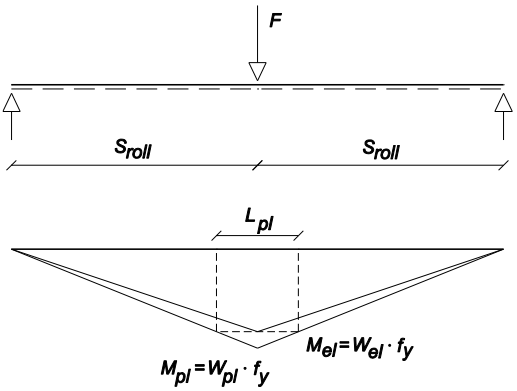

Figure 16: Estimation of the plastic hinge length.

The prescribed displacement at the middle roll should be taken equal to the double of the permanent deflection given by considering the straight beam subjected to three point bending, since the part of the work piece being in the back of the middle roll is not straight but curved. By aggregating also the elastic spring-back deformation, the estimated prescribed displacement at the middle roller is given by Eq. 7.

$$d = 2\left(\frac{S_{roll} \cdot L_{pl}}{2R}\right) + \frac{M_{el} \cdot {S_{roll}}^2}{3EI} \quad (7)$$

Aiming at determining the required prescribed displacement of the middle roller in order to obtain the desired curvatures in the case of the examined arches, the aforementioned formula was employed. Prescribed displacements of 22 mm and 23.5 mm were provided according to Eq. 7 in order to obtain radii of curvatures equal to 4.10 m and 3.71 m respectively; these values were found to provide accurately the desired curvatures for both the low and high arches during the numerical simulation.

3.3 Simulation of the compression and tension tests

Numerical simulation of the compression and tension tests was then performed by employing the restart analysis feature of ADINA; the final condition of the bending process simulation was used as initial condition for the subsequent analysis. This approach was selected in order to take advantage of the reliable residual stress distribution encountered in the specimens, which was obtained from the full curving process simulation. The element-death feature was employed for the finite elements which were not needed any more, such as the ones modelling the rollers, the waste parts of the arches at the starting and ending regions and the contact elements. Rigid links were added to connect the nodes of the edged cross-sections to their geometric centroids, in order to prescribe the boundary conditions (Fig. 17). The semi-rigid stiffness of the supports was introduced with the use of horizontal spring elements at the cross-sectional centroids of the arch ends according to Fig. 12. The support's stiffness in the vertical direction was assumed to be rigid. Either compression or tension loading was applied at the arch's crown with the use of a rigid cylinder, exactly as in the experiments; therefore appropriate contact elements were born using the element-birth feature (Fig. 17). This detailed simulation was selected in order to capture accurately the local buckling of the RHS sections at the location contacting with the rigid cylinder, which was observed in the experiments. A total number of four Geometric and Material Nonlinear Analyses (GMNA) were executed for the low and high arches under tension and compression loading.

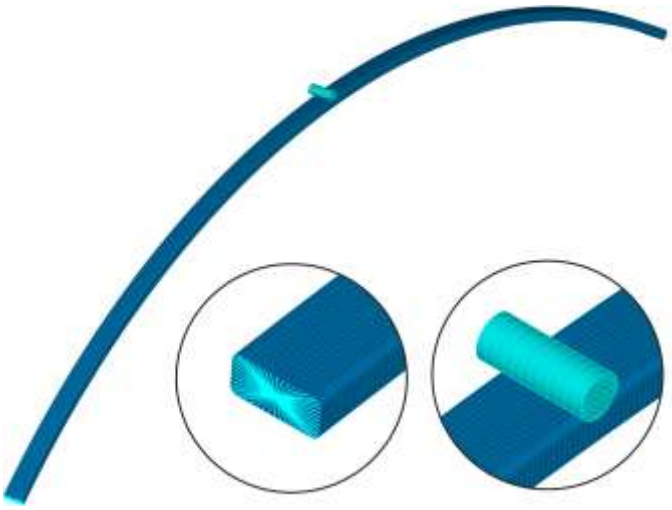

Figure 17: Simulation of the tests and detailed views of the arches boundary and loading conditions.

4. Experimental and numerical results

In this section, the experimental results of the arch specimens (Sp. 1-12) are presented and compared to the corresponding numerical results obtained from Geometric and Material Nonlinear Analyses (GMNA), in terms of equilibrium paths between load and

displacement, developed strains and deformed shapes. Thus, a general overview of the structural behavior is provided and the developed finite element models are validated.

4.1 Compression of high arches

Equilibrium paths relating the imposed load with the vertical displacement at the crown and the transverse displacement at the position of the inclined LVDT are depicted in Fig. 18, concerning the high arches subjected to compression. Excellent agreement is evidenced between the three test results, as all experimental curves almost coincide. The ultimate load capacity is recorded experimentally and numerically equal to 49 kN and 48 kN respectively, although the initial stiffness is numerically overestimated. High arches under compression do not exhibit linear behavior, even for low levels of loading and the ultimate load-bearing capacity is reached by progressive softening, a fact that may be attributed to the effects of the forming process of the rectangular hollow section. The three vertical LVDTs located 150 mm left of the crown, demonstrated that the torsional rotation was prevented with placement of the lateral supports; the LVDTs provided quite similar values to the displacement-cell mounted on the actuator's head. Characteristic strain gauge measurements, including the developed longitudinal strains at the top and bottom flange middle along with the transverse strains at the bottom flange middle, are compared to the corresponding values obtained from GMNA in Fig. 19. The developed longitudinal strains at the top and bottom flange middle are found to exhibit similar magnitudes, while transverse strains are also significant (one quarter of longitudinal strain), which is due to Poisson effect and transverse bending that is typical for curved members. The softening response of the material, which was observed in the equilibrium paths is evidenced in the strain gauge measurements as well. A characteristic deformed shape of this set of test specimens at the end of the experimental and numerical analysis is presented in Fig. 20; local buckling of the top flange is developed at the arches' crown in both cases.

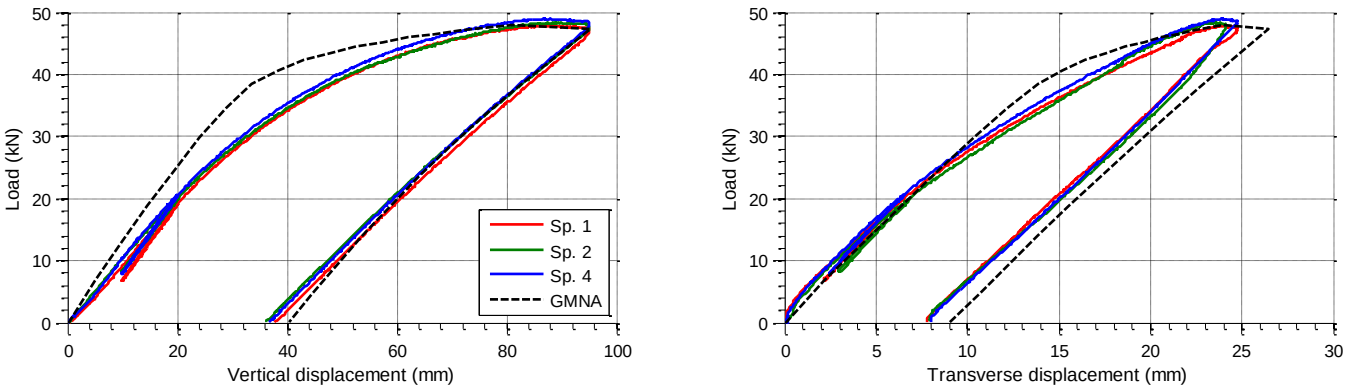

Figure 18: Load-displacement curves at the arch's crown (left) and at ¾ of the span (right).

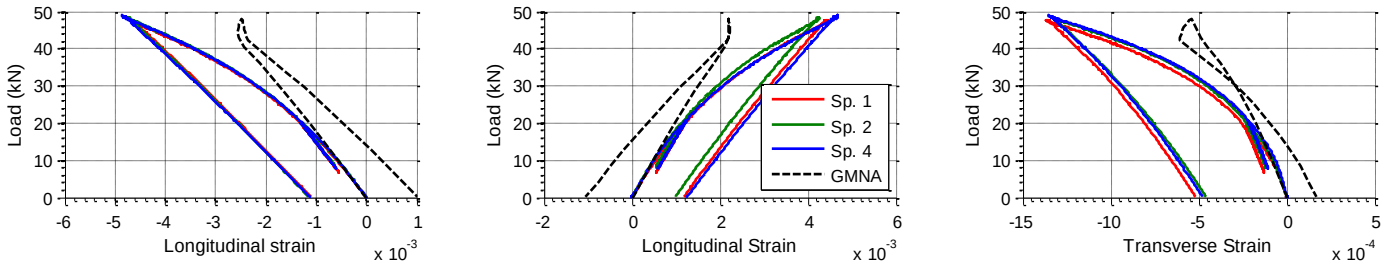

Figure 19: Longitudinal strain at the top flange (left), the bottom flange (middle) and transverse strain at the bottom flange (right).

345

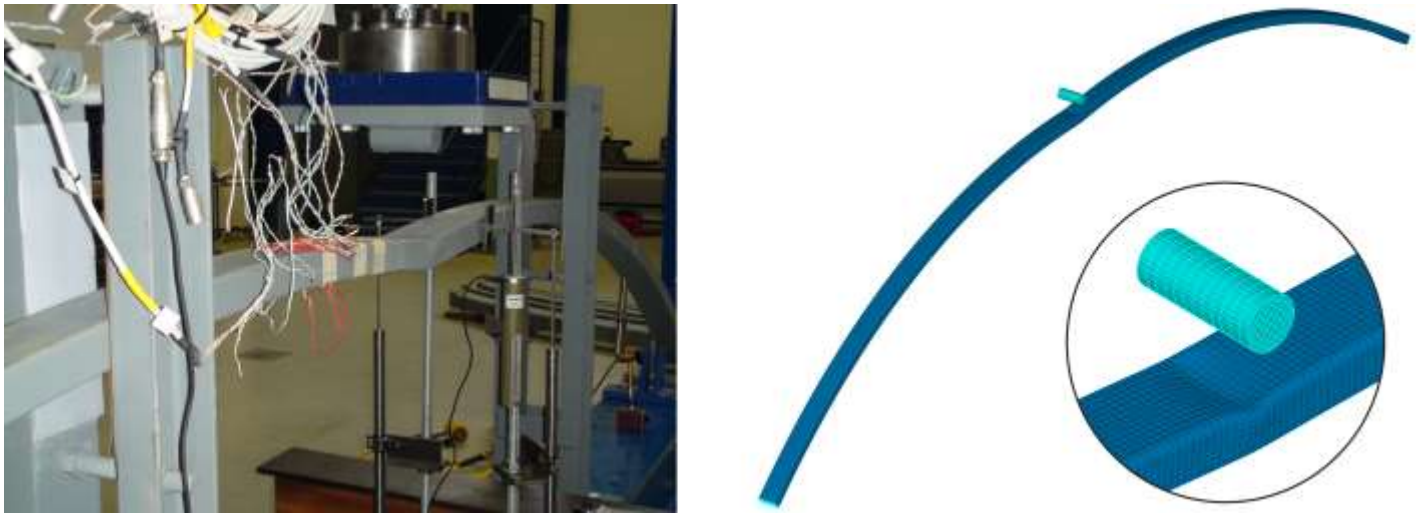

Figure 20: Low arches' deformed shape under compression loading, at the end of test (left) and GMNA (right)

346

347 *4.2 Tension of high arches*

348

349 Experimental and numerical results of the high arches subjected to tension are compared in Fig. 21, in terms of equilibrium paths of
350 the imposed load with the vertical displacement at the crown and the transverse displacement at the position of the inclined LVDT.
351 Excellent agreement is again evidenced again between the three test results. The equilibrium paths in all cases exhibit an initial part of
352 increasing displacement with a small increase of load, which is attributed to the initial geometric tolerances of the support assemblies.
353 Subsequently, an approximately linear response is recorded for imposed load up to 45 kN and it is followed by a gradual diminishing
354 of stiffness until reaching another linear part after 55 kN. Finally at a total displacement of 80 mm, the maximum load is found
355 experimentally and numerically equal to 78.5 kN and 72 kN respectively. Characteristic strain gauge measurements, including the
356 developed longitudinal strains at the top and bottom flange middle along with the transverse strains at the bottom flange middle, are
357 compared to the corresponding values obtained from GMNA in Fig. 22. The developed longitudinal strains at the top and bottom flange
358 middle are found to exhibit similar magnitudes, while transverse strains are also significant. A characteristic deformed shape of this set

of test specimens at the end of experiment and numerical analysis is presented in Fig. 23; in both cases, significant local deformation of the bottom flange is developed at the arches' crown.

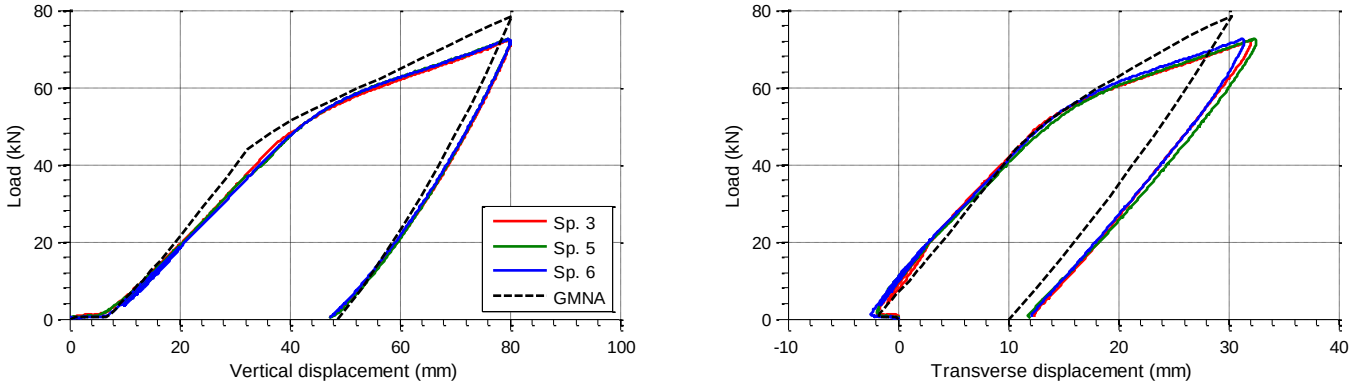

Figure 21: Load-displacement curves at the arch's crown (left) and at ¾ of the span (right).

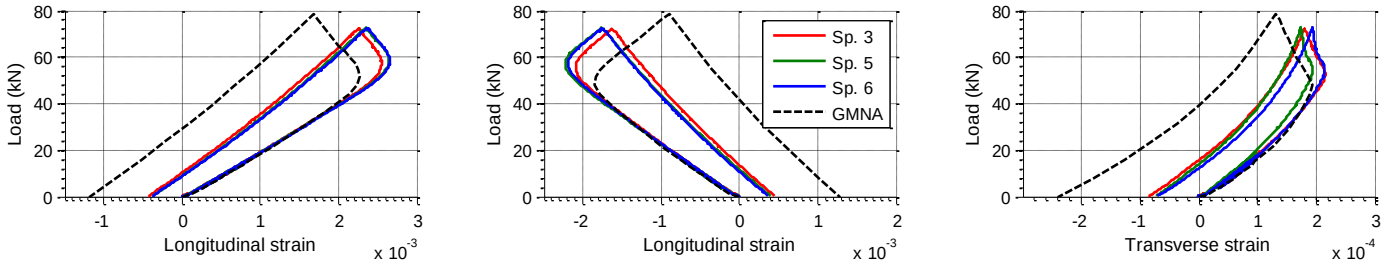

Figure 22: Longitudinal strain at the top flange (left), the bottom flange (middle) and transverse strain at the bottom flange (right).

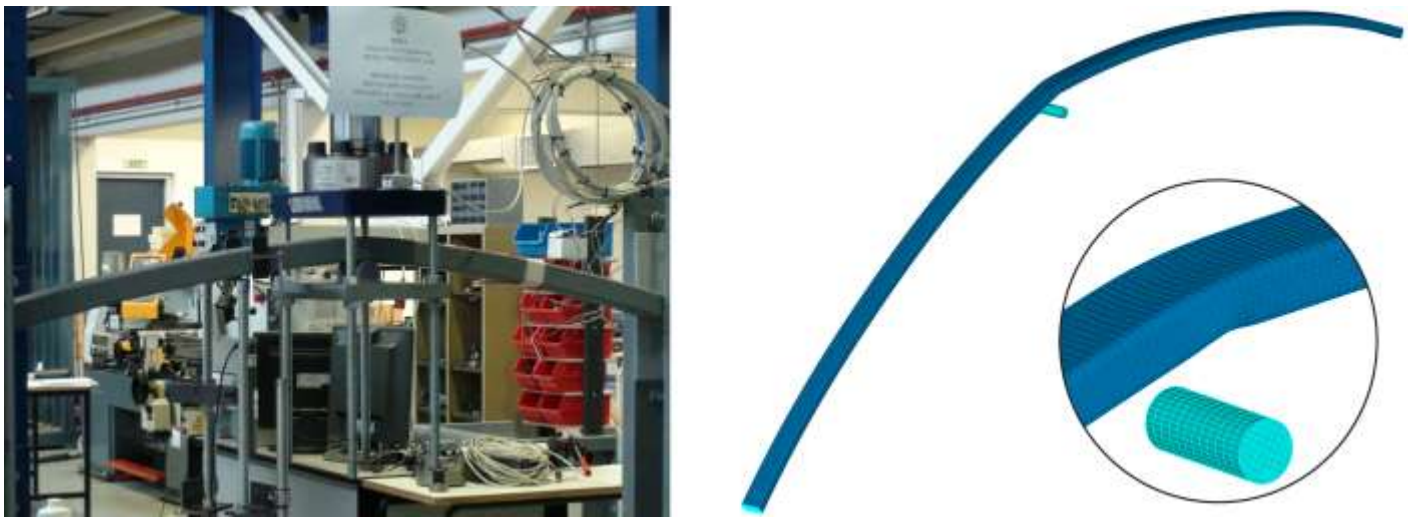

Figure 23: High arches' deformed shape under tension loading, at the end of the test (left) and the GMNA (right)

4.3 Compression of low arches

Equilibrium paths of the imposed load with the vertical displacement at the crown and the transverse displacement at the position of the inclined LVDT are depicted in Fig. 24 concerning the low arches subjected to compression. Specimen 9 failed to support the imposed load due to fracture of the top flange at the crown and the test was stopped prematurely. Furthermore, the loading protocol of Specimen 10 was modified and a total displacement of 150 mm was finally imposed. The response of the low arches under compression is found similar to the corresponding one recorded for the high arches, although in the first case they reach a little lower ultimate load-bearing capacity and exhibit a more flexible response. Stiffness is here predicted by the simulation better than for high arches, which is attributed to the fact that for lower arches geometric non-linearities are more dominant, and considering that geometric nonlinearity is better taken into account in the numerical model than material one. In all cases, the equilibrium paths exhibit an initial part of increasing displacement with a small increase of load, attributed to the initial geometric tolerances of the hinge supports. Characteristic strain gauge measurements, including the developed longitudinal strains at the top and bottom flange middle along with the transverse strains at the bottom flange middle, are compared to the corresponding values obtained from GMNA in Fig. 25. The strain gauge used for measuring longitudinal strains at the top flange middle of Sp. 8 encountered loss of proper contact, which caused stop of recording during the test. The deformed shape at the end of this set of tests is similar to the one depicted for high arches in Fig. 20; the fracture of Sp. 9 at the top flange is shown in Fig. 26.

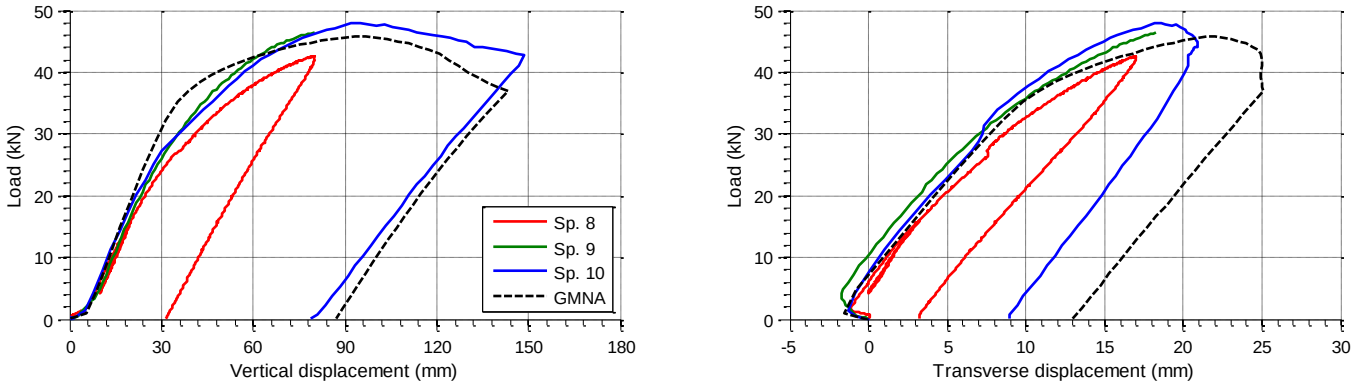

Figure 24: Load-displacement curves at the arch's crown (left) and at ¾ of the span (right).

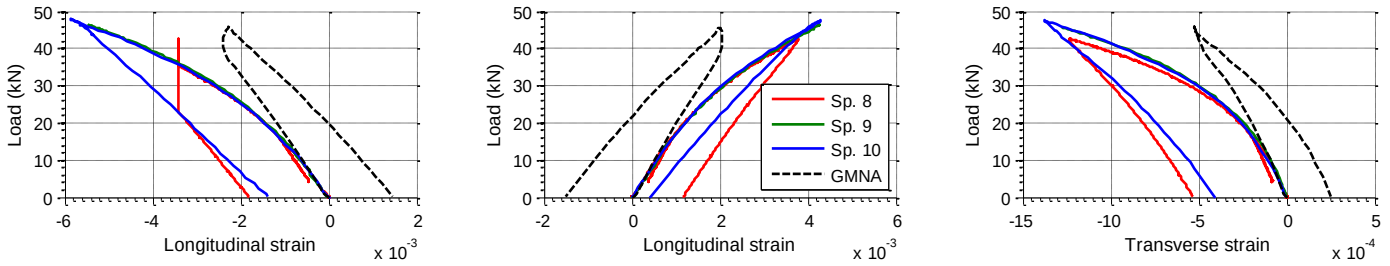

Figure 25: Longitudinal strain at the top flange (left), the bottom flange (middle) and transverse strain at the bottom flange (right).

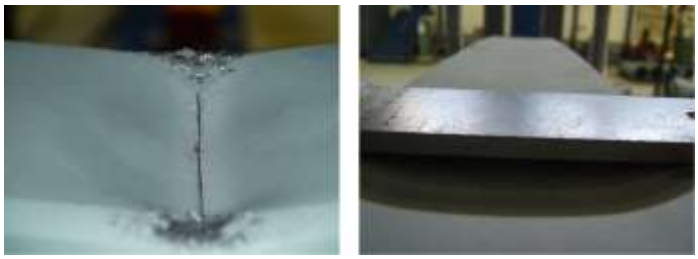

Figure 26:Fracture of Specimen 9, located at the top flange at crown.

4.4 Tension of low arches

The experimental and numerical results of the low arches subjected to tension are compared in Fig. 27, in terms of equilibrium paths of the imposed load with the vertical displacement at the crown and the transverse displacement at the position of the inclined LVDT. Once again, the response of the low arches under tension is similar to the corresponding one recorded for the high arches, although in the first case they reach a little lower ultimate load-bearing capacity and exhibit more flexible response. The inclined LVDTS were not able to measure accurately the transverse displacement of Sp. 12 as the friction between the bottom flange and the LVDT introduced a large amount of errors. Characteristic strain gauge measurements, including the developed longitudinal strains at the top and bottom flange middles, along with the transverse strains at the bottom flange middle, are compared to the corresponding values obtained from GMNA in Fig. 28. The deformed shape of this set of test specimens at the end of the tests is similar to the one depicted for high arches in Fig. 23.

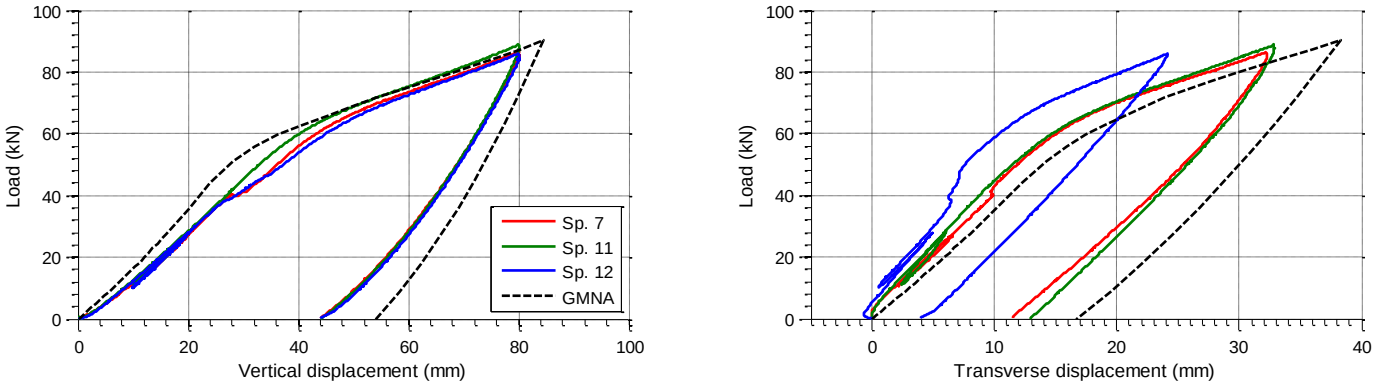

Figure 27: Load-displacement curves at the arch's crown (left) and at ¾ of the span (right).

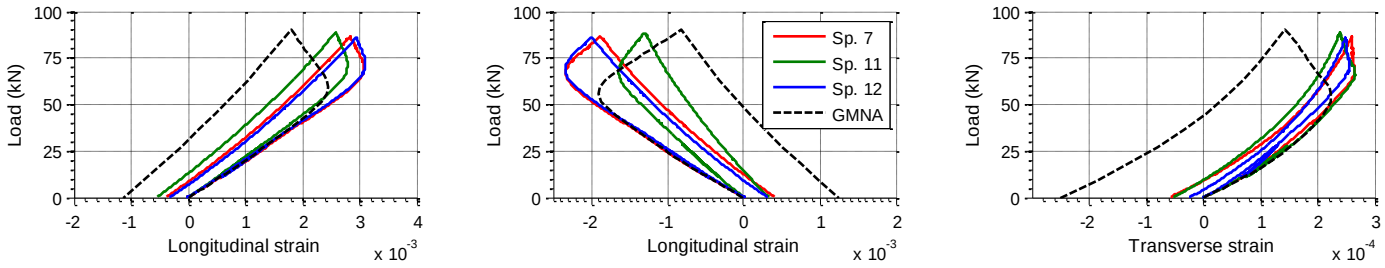

Figure 28: Longitudinal strain at the top flange (left), the bottom flange (middle) and transverse strain at the bottom flange (right).

5. Influence of roller bending on RHS arches

5.1 Residual stress and strain distributions

Overall, a good quantitative and qualitative agreement was achieved between numerical and experimental test results, demonstrating the reliability of the developed finite element models and their ability to estimate the residual stress distribution caused by the forming process. The obtained locked-in stresses along with the developed plastic strains of the low and the high arches at the end of the curving process are illustrated in Fig. 29. All distributions are found to be uniform along the arches, as it is expected due to the constant curvature. A non-symmetrical layout of residual stress and strain is obtained over the cross-sectional width and height; stress and strain concentrations are located at the edges of the bottom flange. The developed strains are reasonably found to be quite larger in the case of high arches compared to low arches. However, in both cases the maximum developed plastic strains are about one order of magnitude larger than the corresponding longitudinal strains that are expected according to the classical beam theory, meaning that the member's remaining ductility is significantly reduced. The obtained stress distribution is found in good agreement with the analytical model proposed in [22].

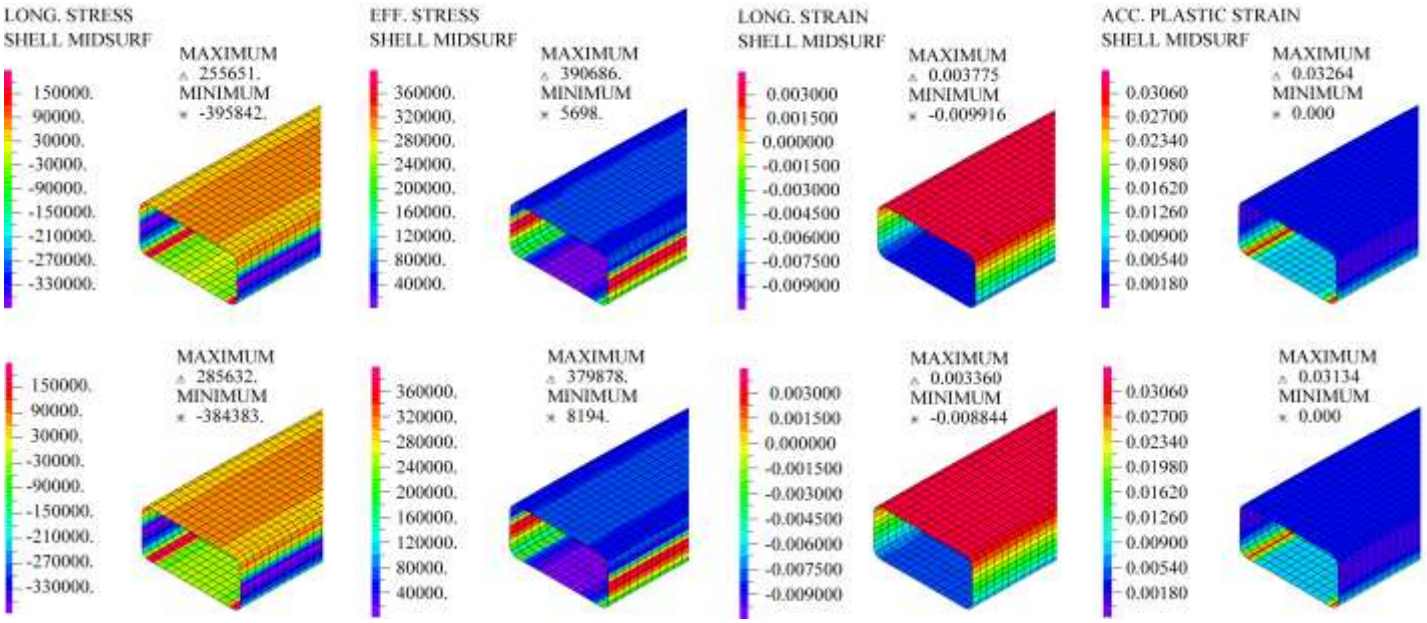

Figure 29: Residual longitudinal stress,von Mises stress, longitudinal strain and accumulated plastic strain of the high (top) and the low arches (bottom).

5.2 Comparison of the overall response

During typical structural analysis and design of arches, it is difficult to take into consideration residual stresses emanating from the manufacturing process. In practice, arched structures are usually subjected to compressive distributed loads with either radial or gravity direction. Since the developed numerical models, incorporating the computed residual stresses, have been validated from the experimental results, they were next employed for evaluating the influence of residual stresses on the overall structural response. To that end, two additional numerical models were developed, using the same nodal mesh geometries with the high and low arches after the curving process. A uniform and sufficiently dense mesh with 4-node shell elements and five integration points at the element thickness direction was chosen and a bilinear material model based on the mechanical properties obtained from tensile coupon tests (Section 2.2) was employed once again. Geometry and material nonlinear analyses were carried out in all cases, under uniform compressive loading at the top flange with either radial or vertical direction. The obtained equilibrium paths of the high and low arches with and without residual stresses are compared in Fig. 30, in terms of the imposed load and the corresponding vertical displacement at the crown. In all cases, the initial stiffness and the ultimate strength capacity of the low arches are found reasonably lower compared to the high arches. Residual stresses are evidenced to have a positive impact on the ultimate strength capacity under vertical loading, increasing the load-bearing capacity by approximately 10%. On the other hand, residual stresses have a negligible effect on the structural response of the arches under radial loading, where the load is carried largely in axial compression.

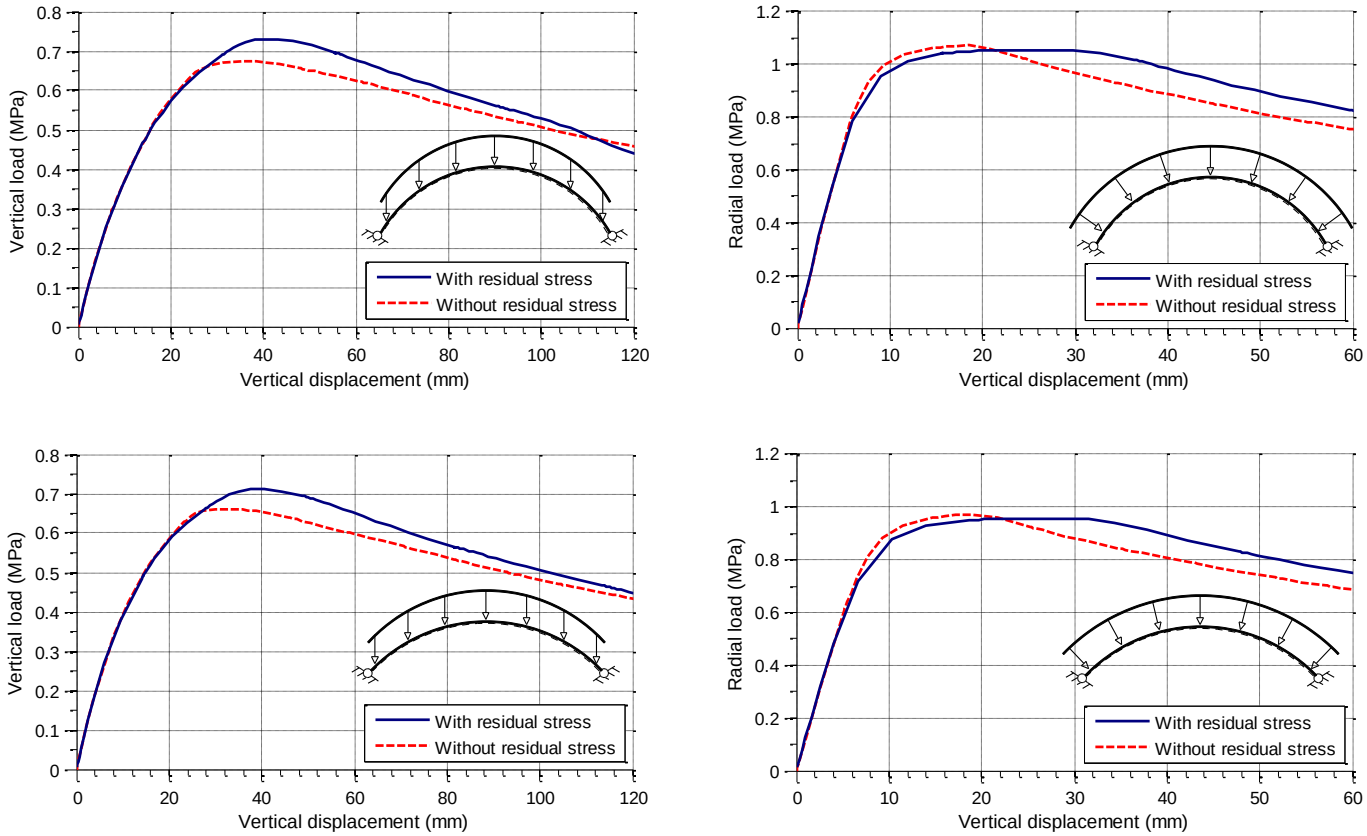

Figure 30: Equilibrium paths of the high (top) and low (bottom) arches, under compression loading at the vertical (left) and radial (right) directions.

6. Conclusions

The influence of the curving process on rectangular hollow section steel arches has been assessed in the present study. Twelve circular arches, grouped in two sets of curvatures, were tested under tension and compression loading. Finite element models were used to simulate in detail the curving procedure and then the experimental tests and implicit static analyses accounting for geometric and material nonlinearities were carried out. An analytical formula for estimating the required displacements of the bending machine rollers in order to obtain the desired curvature was also proposed, which can support both the numerical simulation and the manufacturing procedure. Experimental and numerical results were compared in terms of load-displacement equilibrium paths, strain-gauge measurements and deformed shapes. Quite good agreement was observed regarding the load-displacement curves and the deformed shapes, while some discrepancies were observed in the strain gauge measurements. Overall, a quite good quantitative and qualitative agreement was achieved between FEA and experimental test results, demonstrating the reliability of the developed finite element models, which are hence capable of estimating the residual stress distribution caused by the forming process.

The numerically estimated residual stresses and strains were presented for the two sets of arches demonstrating similar distributions in both cases; the patterns differed significantly from those obtained by applying opposite prescribed rotations at the beam's ends and therefore modelling of the exact bending procedure is considered to be mandatory for proper estimation of such stresses. The maximum accumulated plastic strains were found to be remarkably larger than the developed longitudinal strains, meaning that the member's remaining ductility has been significantly reduced during roller bending. Additionally, the developed strains were found to increase with increasing arch curvature. The influence of the curving process on the overall structural response has been assessed for the arches subjected to compressive distributed loading with either radial or gravity direction, which are the most common cases encountered in engineering practice. In the case of the arches subjected to gravity loading, the ultimate strength capacity when considering the residual stresses was found to be increased by approximately 10%, while in the case of the arches subjected to radial loading, residual stresses had a negligible effect on the overall behaviour.

Acknowledgements

The authors gratefully acknowledge the financial support of the State Scholarships Foundation in the frame of the Research Projects of Excellence IKY/Siemens. The second author would like to acknowledge support by the European Community under a Marie Curie Intra-European Fellowship for Career Development (Grant agreement number 235196).

Appendix A. Dimensions of specimens, best fitting radii and deviations.

The measured dimensions of each specimen, including the length of the horizontal span (L), the height at five locations along the member (h_1-h_5) and the corresponding values of the theoretical form, are summarized in tables A1 and A2, for the high and low arches respectively.

Table A1. High arches dimensions.

Arches	L (mm)	h_1 (mm)	h_2 (mm)	h_3 (mm)	h_4 (mm)	h_5 (mm)
Sp. 1	4726	453	735	825	736	454
Sp. 2	4738	449	723	811	728	454
Sp. 3	4737	458	730	815	729	456
Sp. 4	4734	453	734	821	728	452
Sp. 5	4730	455	732	827	737	458
Sp. 6	4728	467	740	832	739	464
Average	4732	456	732	822	733	456

Theoretical	4725	459	737	825	737	459

Table A2. Low arches dimensions.

Arches	L (mm)	h_1 (mm)	h_2 (mm)	h_3 (mm)	h_4 (mm)	h_5 (mm)
Sp. 7	4709	406	654	736	652	401
Sp. 8	4706	409	659	739	661	407
Sp. 9	4725	403	648	723	643	394
Sp. 10	4716	400	659	740	659	402
Sp. 11	4707	402	659	744	660	398
Sp. 12	4711	405	657	739	654	401
Average	4712	404	656	737	655	401
Theoretical	4725	397	645	724	645	397

The best fitting radius and the deriving deviations of each specimen's curvature, obtained by employing the least square method, are presented in tables A3 and A4, for the high and low arches respectively.

Table A3. Best fitting radii and deviations of high arches.

Arches	Best fitting radius (mm)	St. deviation (mm)	Min. deviation (mm)	Max. deviation (mm)
Sp. 1	3708	2.6	-3.6	2.7
Sp. 2	3776	2.1	-2.7	3.3
Sp. 3	3761	1.1	-1.2	1.8
Sp. 4	3733	2.9	-3.0	3.0
Sp. 5	3700	3.0	-3.9	3.9
Sp. 6	3700	2.4	-2.9	3.6
Average	3730	2.4	-2.9	3.0

Table A4. Best fitting radii and deviations of low arches.

Arches	Best fitting radius (mm)	St. deviation (mm)	Min. deviation (mm)	Max. deviation (mm)
Sp. 7	4031	2.3	-2.4	4.3
Sp. 8	4007	2.3	-2.5	3.3
Sp. 9	4109	3.4	-2.6	5.6
Sp. 10	4014	1.9	-3.3	1.5
Sp. 11	3986	2.8	-4.7	2.9
Sp. 12	4022	1.8	-2.4	2.1
Average	4028	2.4	-3.0	3.3

References

[1] Bjorhovde R. Cold bending of wide-flange shapes for construction. Engineering Journal 2006;43(4):271-86.

[2] C. King, D. Brown, Design of Curved Steel, The Steel Construction Institute, Berkshire, 2001.

[3] Weisenberger G. Bending in the right direction. Modern Steel Construction 2007;(5).

[4] Alwood TA. What engineers should know about bending steel. Modern Steel Construction 2006;(5).

[5] J.B. Kennedy, Minimum Bending Radii for Square & Rectangular Hollow Sections (3-roller Cold Bending), CIDECT Report 11C-88/14, 1988.

[6] J.F. Brady, Determination of Minimum Radii for Cold Bending of Square and Rectangular Hollow Structural Sections, CIDECT Report 11B-78/12, 1978.

[7] J.B. Kennedy, Deformations of Hollow Structural Sections Subjected to Cold Bending, CIDECT Report 11Bt-85/2, 1985.

[8] AISC, Steel Construction Manual, 13th Ed.,USA, 2006

[9] ECCS. Manual on stability of steel structures - ECCS Committee 8 Stability: 1976.

[10] Young BW. Residual stresses in hot rolled members. IABSE Reports of the Working Commissions 1975;23:2538.

[11] Galambos TV. Guide to stability design criteria for metal structures. New York: John Wiley & Sons Inc.; 1998.

[12] Alpsten G. Residual stresses, yield stress, and the column strength of hot- rolled and roller-straightened steel shapes. IABSE Reports of the Working Commissions 1975;23:3959.

[13] Kato B, Aoki H. Residual stresses in cold-formed tubes. Journal of Strain Analysis 1978;13(4):193204.

[14] Weng CC, White RN. Residual stresses in cold-bent thick steel plates. Journal of Structural Engineering ASCE 1990;116(1):2439.

[15] Weng CC, Pekoz T. Residual stresses in cold-formed steel members. Journal of Structural Engineering ASCE 1990;116(6):161125.

[16] C.D. Moen, T. Igusa, B.W. Schafer, Prediction of residual stresses and strains in cold-formed steel members, Thin-Walled Struct. 46 (2008) 1274–1289. doi:10.1016/j.tws.2008.02.002.

[17] M. Abambres and W.-M. Quach, Residual stresses in steel members : a review of available analytical expressions, International Journal of Structural Integrity 7 (2016). doi:10.1108/IJSI-12-2014-0070.

[18] S.P. Timoshenko, Strength of Materials: Part II: Advanced Theory and Problems, 2 ed.D. Van Nostrand Company, Inc., N. Y., 1940

[19] R.C. Spoorenberg, H.H. Snijder, J.C.D. Hoenderkamp, Experimental investigation of residual stresses in roller bent wide flange steel sections, J. Constr. Steel Res. 66 (2010) 737–747.

[20] R.C. Spoorenberg, H.H. Snijder, J.C.D. Hoenderkamp, Finite element simulations of residual stresses in roller bent wide flange sections, J. Constr. Steel Res. 67 (2011) 39–50.

[21] R.C. Spoorenberg, H.H. Snijder, J.C.D. Hoenderkamp, Proposed residual stress model for roller bent steel wide flange sections, J. Constr. Steel Res. 67 (2011) 992–1000.

[22] S.P. Chiew, Y.F. Jin, C.K. Lee, Residual stress distribution of roller bending of steel rectangular structural hollow sections, JCSR. 119 (2016) 85–97. doi:10.1016/j.jcsr.2015.12.016.

[23] Y.L. Pi, N.S. Trahair, In-plane inelastic buckling and strengths of steel arches, J. Struct. Eng. 122 (7) (1996).

[24] Y.L. Pi, N.S. Trahair, Inelastic lateral buckling strength and design of steel arches, Eng. Struct. 22 (2000) 993–1005.

[25] Komatsu S, Sakimoto T. Ultimate load carrying capacity of steel arches. Journal of the Structural Division 1977;103(12):2323-36.

[26] M. Hadjioannou, C. Douthe, C.J. Gantes, Influence of Cold Bending on the Resistance of Wide Flange Members, 13 (2013) 353–366. doi:10.1007/s13296-013-2013-6.

[27] ADINA System Release Notes. ADINA R&D Inc. Watertown. U.S.A.; 2017.

[28] EN ISO 6892-1:2009,MetallicMaterials – Tensile Testing – Part 1:Method of Test at Room Temperature, March 2009.

[29] P.W. Key, G.J. Hancock, A Theoretical Investigation of the Column Behaviour of Cold-Formed Square Hollow Sections, Thin-Walled Structures, vol. 16, pp. 31-64, 1993.

[30] Gantes CJ, Fragkopoulos KA. Strategy for Numerical Verification of Steel Structures at the Ultimate Limit State. Struct & Infrastruct Eng 2010;6:225–255.